

Article

Cluster Hardening Effects on Twinning in Mg-Zn-Ca Alloys

Ruixue Liu ¹, Jie Wang ¹, Leyun Wang ^{1,2,*} , Xiaoqin Zeng ^{1,2,*} and Zhaohui Jin ³

¹ National Engineering Research Center of Light Alloy Net Forming, Shanghai Jiao Tong University, Shanghai 200240, China; liurx1221@163.com (R.L.); 18217278361@163.com (J.W.)

² State Key Laboratory of Metal Matrix Composites, Shanghai Jiao Tong University, Shanghai 200240, China

³ Shenyang National Laboratory for Materials Science, Institute of Metal Research, Chinese Academy of Sciences, 72 Wenhua Road, Shenyang 110016, China; zhjin@imr.ac.cn

* Correspondence: leyunwang@sjtu.edu.cn (L.W.); xqzeng@sjtu.edu.cn (X.Z.)

Abstract: Twinning is a critical deformation mode in Mg alloys. Understanding deformation twinning (DT) is essential to improving mechanical properties of Mg alloys. To address the experimentally observed conspicuous hardening effects in Mg-1.8Zn-0.2Ca alloys, interactions between the {10–12} twin boundaries (TBs) and solute clusters in Mg-Zn-Ca alloys were examined via molecular dynamics (MD) simulations. We find that the Zn/Ca-containing clusters show different hindering effects on TBs and an increment in the applied shear stress of 100 MPa is required to accomplish the interaction between the boundary and the cluster with Ca content > 50 at%. The cluster hardening effects on twinning are positively correlated to the Ca content and the size of the clusters in Mg-Zn-Ca alloys.

Keywords: Mg-Zn-Ca alloy; twin boundary; solute cluster hardening; molecular dynamics simulation



Citation: Liu, R.; Wang, J.; Wang, L.; Zeng, X.; Jin, Z. Cluster Hardening Effects on Twinning in Mg-Zn-Ca Alloys. *Metals* **2022**, *12*, 693. <https://doi.org/10.3390/met12040693>

Academic Editor: Eric Hug

Received: 28 January 2022

Accepted: 9 March 2022

Published: 18 April 2022

Publisher's Note: MDPI stays neutral with regard to jurisdictional claims in published maps and institutional affiliations.



Copyright: © 2022 by the authors. Licensee MDPI, Basel, Switzerland. This article is an open access article distributed under the terms and conditions of the Creative Commons Attribution (CC BY) license (<https://creativecommons.org/licenses/by/4.0/>).

1. Introduction

Lightweight magnesium (Mg) alloys are in the spotlight for energy efficiency for transportation applications [1,2]. Deformation twinning (DT) on the {1012} (1011) system is an important plastic deformation mechanism in Mg with a hexagonal crystal structure. Nucleation and growth of twins are responsible for hardening and texture evolution characteristics, and ultimately influence the mechanical properties and formability of Mg and its alloys [3,4].

Once they are nucleated, deformation twins usually propagate quickly by moving the twin boundaries across the matrix grain. This process corresponds to a stage on the stress–strain curve with near-zero strain hardening. Introducing microscopic barriers to hinder the motion of twin boundaries (TBs) is an effective way to strengthen Mg alloys [5–7]. Some studies suggested that the segregation of certain solute atoms to the TBs can exert a strong pinning effect on the migration of TBs, resulting in a significant enhancement in hardness and mechanical strength [8–10]. The solute/TB interaction can even serve as a new atomic-scale mechanism for dynamic strain aging [11]. Interactions between TBs and precipitates of various shapes (e.g., basal plates, prismatic plates, c-rods) have also been examined by both experimental and computational approaches to elucidate the strengthening effect of those precipitates [12–15]. On the other hand, little attention has been paid to the interaction between TBs and solute clusters, which are somewhere between single solute atoms and crystallized precipitates.

Clusters are recognized to form in the early stages of precipitation and have a vital influence on mechanical properties of Mg-RE alloys, such as Mg-Y and Mg-Gd alloys [16,17]. Gd-rich clusters are found to segregate onto high-angle grain boundaries, which leads to the grain refinement and texture weakening in Mg-Gd alloys [17]. Clusters of non-RE elements have been less well studied. Recently, Ca-containing Mg alloys have received strong attention because of their excellent mechanical properties and low fabrication cost [18–22]. In particular, Mg-Zn-Ca alloys demonstrate ultra-high ductility and moderate texture [23–27]. Those

features are often attributed to the co-segregation of Zn and Ca atoms onto grain boundaries (GBs), which is believed to enhance GB cohesion. On the other hand, how Zn-Ca clusters would affect the deformation mechanisms in the grain interior is not well understood. In the present work, we study the interaction between Zn-Ca clusters and TBs by molecular dynamics (MD) simulations. The result will help us better understand the work hardening behavior of Mg-Zn-Ca alloys.

2. Experimental Methods

2.1. Material Synthesis

A moderate-textured Mg-1.8Zn-0.2Ca (wt.%) alloy (denoted as ZX20) was casted and extruded. The ZX20 alloy was made from pure Mg, pure Zn, and Mg-20 wt.% Ca master alloy in an electric resistance furnace under protective gas consisting of CO₂ (99 vol.%) and SF₆ (1 vol.%). The melt was poured into a cylindrical steel mold preheated to 200 °C and then naturally cooled in air. The actual chemical composition of the cast billets was determined by an inductively coupled plasma atomic emission spectroscopy (ICP-AES) analyzer (Perkin-Elmer, Plasma 400, Norwalk, CT, USA). The cast billets were machined into cylindrical samples 60 mm in diameter and 70 mm in height, followed by homogenization at 400 °C for 12 h. One-step direct extrusion was carried out at 250 °C and 2 mm/s to produce round bars of 14 mm in diameter, which corresponds to an extrusion ratio of ~18:1.

2.2. Microstructural Characterization and Mechanical Test

Microstructures of the alloy were characterized with electron backscattered diffraction (EBSD) and transmission electron microscopy (TEM). The surface of the sample was mechanically ground using sandpapers and then electro-polished in an ethanol–10% perchloric acid electrolyte for EBSD characterization. TEM was employed to characterize finer microstructures in the alloy using a JEM-ARM200F instrument (JEOL Ltd., Tokyo, Japan). More details of EBSD and TEM analysis can be found in Refs [28,29].

Dog-bone tensile specimens with gauge dimensions of 18.0 mm × (L) × 4.8 mm (W) × 1.4 (T) were machined from the extruded alloys for standard tension tests. Cylindrical specimens with a diameter of 5 mm and a height of 7.5 mm were used for compression tests. The loading axes in tension tests were parallel to the extrusion direction while the compression tests were conducted with loading axes 0, 45, and 90 degrees from the extrusion direction. The tension and compression tests were conducted with crosshead speeds of 0.5 and 0.2 mm/min, respectively, which corresponds to a nominal strain rate of $\sim 5 \times 10^{-4} \text{ s}^{-1}$ in both tests.

2.3. Experimental Observations

As the solute Ca is dilute in this alloy, precipitates such as Mg₂Ca are not readily formed. A rich profusion of solute clusters in various sizes were found to distribute uniformly in the matrix, as revealed by high-angle annular dark field-scanning transmission electron microscopy (HAADF-STEM) as shown in Figure 1. Since the brightness of individual atomic columns in the HAADF-STEM image is proportional to the square of the averaged atomic number, each bright dot in Figure 1 represents a Zn/Ca-rich column. The presence of solute clusters rather than precipitates in the cast and as-extruded ZX20 alloy is likely the result of low extrusion temperature (250 °C) and high extrusion speed (2 mm/s) which tend to suppress the dynamic precipitation.

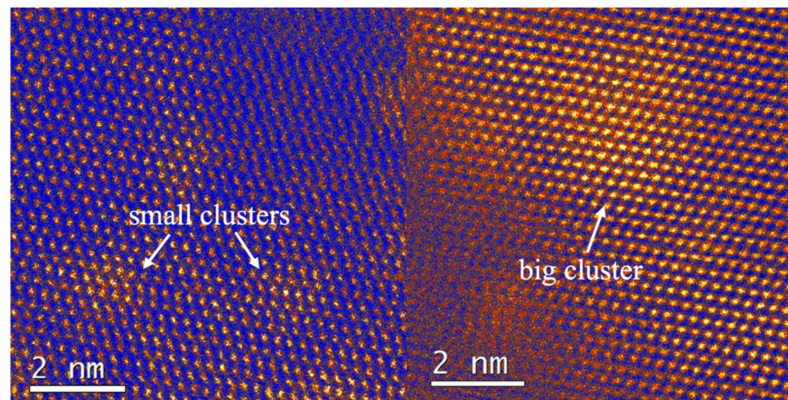


Figure 1. HAADF-STEM images showing atomic clusters in the Mg-1.8Zn-0.2Ca alloy.

For the as-extruded ZX20 alloy, a tension–compression (T-C) asymmetric behavior [30–32] is observed. As shown in Figure 2, the stress–strain curve obtained from tensile tests along the extrusion direction (ED) differs strongly from that obtained from compressive tests along the ED. The tensile yield strength (TYS \approx 150 MPa) was higher than the compressive yield strength (CTS \approx 100 MPa). Yet, the stress level during the compression test increased rapidly after 2% strain, and the ultimate compressive strength (UCS \approx 500 MPa) was much higher than the ultimate tensile strength (UTS \approx 300 MPa).

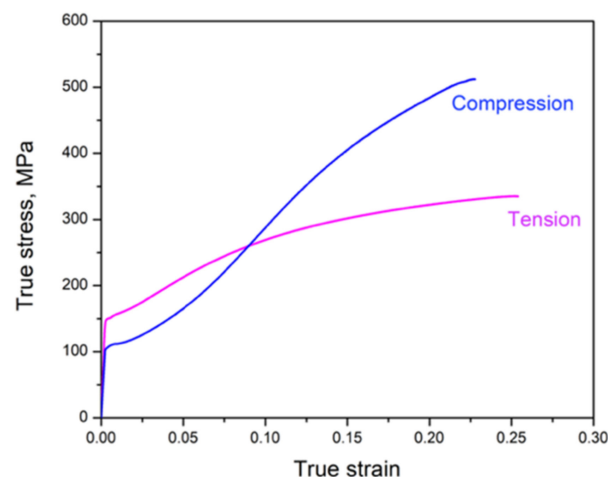


Figure 2. Stress–strain curves of the as-extruded ZX20 alloy deformed in tension and compression along ED.

The T-C asymmetry in the ZX20 alloy is attributed to the more frequent nucleation of deformation twins $\{10\bar{1}2\}$ in the compression test than that in the tension test. The ZX20 alloy exhibits a moderate extrusion texture (Figure 3). The $\{10\bar{1}2\}$ twinning would be suppressed under tension along the ED, but be favored under compression along the ED. However, compared to other as-extruded Mg alloys, such as AZ31, MN11, and Mg-5wt.%Y [33–35], the ZX20 alloy exhibits a much stronger hardening in the compressive stress–strain curve, which suggests that the growth of twins must have met some resistance. The above experimental observations motivated us to study the interaction between TBs and Zn-Ca solute clusters.

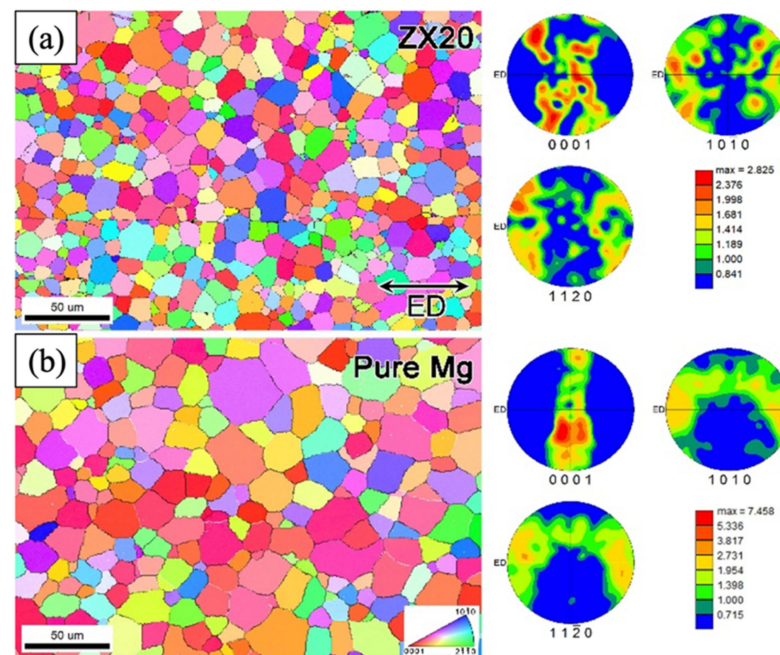


Figure 3. Inverse pole figure (IPF) maps and pole figures (PFs) of (a) ZX20 and (b) pure Mg. The colors in the IPF maps represent the grain orientations with respect to the extrusion direction (adapted from [28]).

3. Computational Procedures

MD simulations were carried out to investigate the cluster–twin interaction in the ZX20 alloy. The simulations were performed using the open-source code “LAMMPS” [36]. The modified embedded-atom method (MEAM) interatomic potential developed by Jang et al. [37] for the Mg–Zn–Ca ternary system was utilized. The visualization tool Ovito [38] was used for analyzing the simulation data, and atoms were colored by atom type as indicated in the legend of each figure containing an MD snapshot. In particular, with the common neighbor analysis (can) in Ovito, atoms at defect sites such as grain boundaries, dislocations, and faults were distinguished.

The MD sample illustrated in Figure 4 contained 821,530 atoms, having dimensions of 55 nm × 52 nm × 4.5 nm. A pair of $\{10\bar{1}2\}$ TBs at a separation distance of 32 nm were introduced within the MD supercell under three-dimensional (3D) periodic boundary conditions. The lower TB was fixed by periodically replacing Mg atoms at compression GB sites with Zn atoms such that the interaction with the cluster only involved the upper TB (the TB moving toward the cluster) [8]. To avoid additional size effects in 3D, the shapes of clusters were chosen to be cylindrical with length equal to that of the MD box in the Z direction. The cluster size was measured by the radius R of the circular cross-section. Clusters containing different Zn and Ca contents were produced by randomly replacing Mg atoms by Zn and Ca atoms at a certain Zn/Ca ratio in the cluster domain.

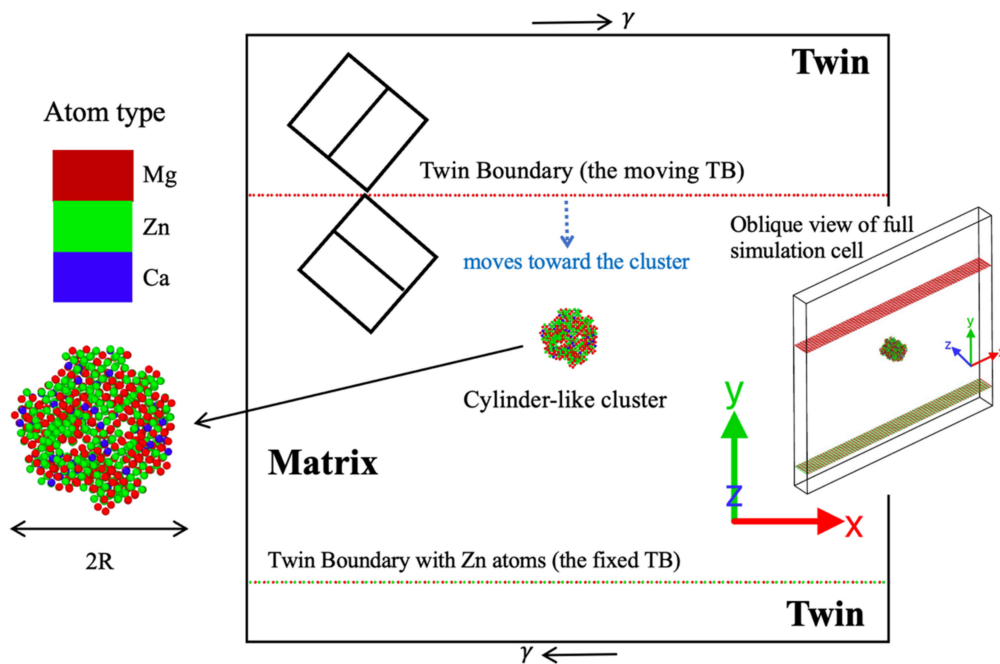


Figure 4. MD simulation supercell with a pair of horizontal TBs in Mg lattice and a Zn-Ca-containing cylinder-shaped column (cluster) residing 15 nm below the upper TB. Zn atoms (colored green) had been introduced to the lower TB sites to replace Mg atoms periodically, such that only the upper TB tended to migrate downward when the MD box was deformed by applying an X–Y plane simple shear at a constant rate. The MD supercell was $55 \times 52 \times 4.5 \text{ nm}^3$ under the 3D periodic boundary conditions. Both the Zn/Ca ratio and the size of the cluster could be varied in our study. Atoms sitting at perfect hcp lattice sites are not shown.

Local strains and stresses were generated due to mismatch in atomic size which was most significant when Ca was introduced. The contents of Ca and Zn in the cluster zone were therefore limited to avoid unexpected defect nucleation, such as dislocations and stacking faults. Thus, only 30% Mg atoms of clusters were set to be replaceable in this study, and the Zn/Ca ratios and radius of clusters were chosen to be $x:y \in [0:10, 1:9, 5:5, 9:1, 10:0]$ and $R \in [1.5, 2.5, 4.0] \text{ nm}$, respectively. In this case, the Zn/Ca ratio (indicated as $x\text{Zn}_y\text{Ca}$ in the following parts, i.e., 10Zn , $1\text{Zn}9\text{Ca}$, $9\text{Zn}1\text{Ca}$, etc.) refers only to the 30% replaceable Mg atoms, irrespective of other Mg atoms.

Energy minimizations were performed on the entire supercell to relax the TB and the cluster. The isothermal–isobaric (NPT) ensemble was then employed to increase the temperature to 300 K at a time interval of 200 ps in zero-pressure conditions and the state was further relaxed at the same temperature by 100 ps with the canonical (NVT) ensemble. Then, simple shear strain was applied in the microcanonical (NVE) ensemble at a strain rate of $1 \times 10^8/\text{s}$, which was slow enough to avoid artificial kinetic effects according to previous MD simulations [39–41]. The simple shear was applied in the X–Y plane to provide a driving force in accordance with the twinning shear to move the TB in the negative Y direction towards the cluster. A timestep of 0.001 ps was used in the MD simulations and the stress, total energy, and atomic position data were stored every 1 ps. To eliminate thermal noises, all figures were exported after performing conjugate gradient energy minimizations for 5ps to eliminate thermal fluctuation of the atomic structure and atoms at perfect Mg lattice sites were hidden for better observation [42].

4. Results and Discussion

4.1. Effect of the Zn/Ca Ratio

To clarify how cluster-hardening effects depend on the Zn/Ca ratio, a set of clusters with fixed radius $R = 2.5$ nm were considered. The corresponding stress–strain curves obtained by MD simulations are shown in Figure 5. The cluster-free case is taken as a reference for comparison. Due to the X–Y deformation in current simulations, the shear stress is computed as the sum value of the per-atom τ_{xy} in the MD supercell, while the shear strain is defined as $\Delta L/L_0$, where ΔL is the displacement distance in the X direction from the unstrained orientation and L_0 is the box length in the Y direction. It is worth noting that since twinning is the only mode of plastic deformation due to the absence of lattice dislocations or other defects, the yield stress defines the critical resolved shear stress (CRSS) for TB migration [43,44].

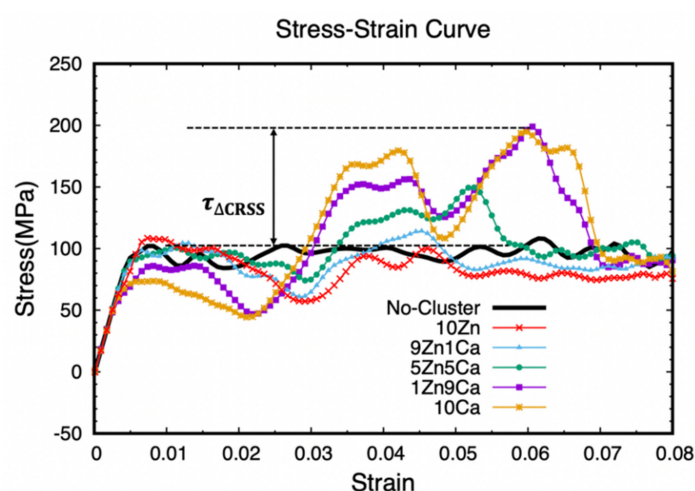


Figure 5. Shear stress–strain curves for clusters having different Zn/Ca ratios when they are sheared by the upper TB.

According to the stress–strain curves, the CRSS of TB migration is found to be ~ 100 MPa for the cluster-free case, and the subsequent flow stress stays at nearly the same level, indicating that there is hardly any strain hardening effect in the Mg lattice. When clusters are present, the yield points are found to differ significantly. For Zn-rich clusters (i.e., 9Zn1Ca, or 10Zn), the yield stress and the subsequent flow stress are also close to 100 MPa, suggesting a weak cluster pinning effect on TB. On the contrary, the yield stress and the subsequent flow stress apparently decreased with Ca-rich clusters (i.e., 1Zn9Ca or 10Ca), indicating that an attraction force has been imposed on the TB, which is probably caused by lattice distortions due to the large atom size of Ca. A similar attraction force was also observed between precipitates and an approaching TB in a recent study [45]. Then, immediately, a hump-like stress–strain response is observed when the TB migration is temporarily blocked by the Ca-rich cluster after their interaction. This essentially applies a hardening effect, which can be quantified by $\tau_{\Delta CRSS}$ defined as the difference between the peak flow stress in the presence of clusters and the flow stress in the cluster-free case (Figure 5). It is found that the $\tau_{\Delta CRSS}$ value increases from ~ 10 MPa to nearly 100 MPa as the Ca:Zn ratio rises from 1:9 to 10:0.

According to the stress–strain curves in Figure 5, a work hardening coefficient about 2000 MPa ($\theta = d\sigma/d\varepsilon$) was calculated [46–48] for the 1Zn9Ca and 10Ca cases, and about 1000 MPa for the 5Zn5Ca case. The ZX20 alloy actually has a θ value of about 750 MPa, which is comparable to the above computational values.

The interactions between a migrating TB and two clusters in different Zn/Ca ratios, 9Zn1Ca and 1Zn9Ca, are depicted in Figure 6a,b. After the onset of plastic yielding, the TB

starts migrating towards the cluster by the glide of twinning dislocations, as shown for the T1 step in Figure 6, in agreement with previous MD simulations [45].

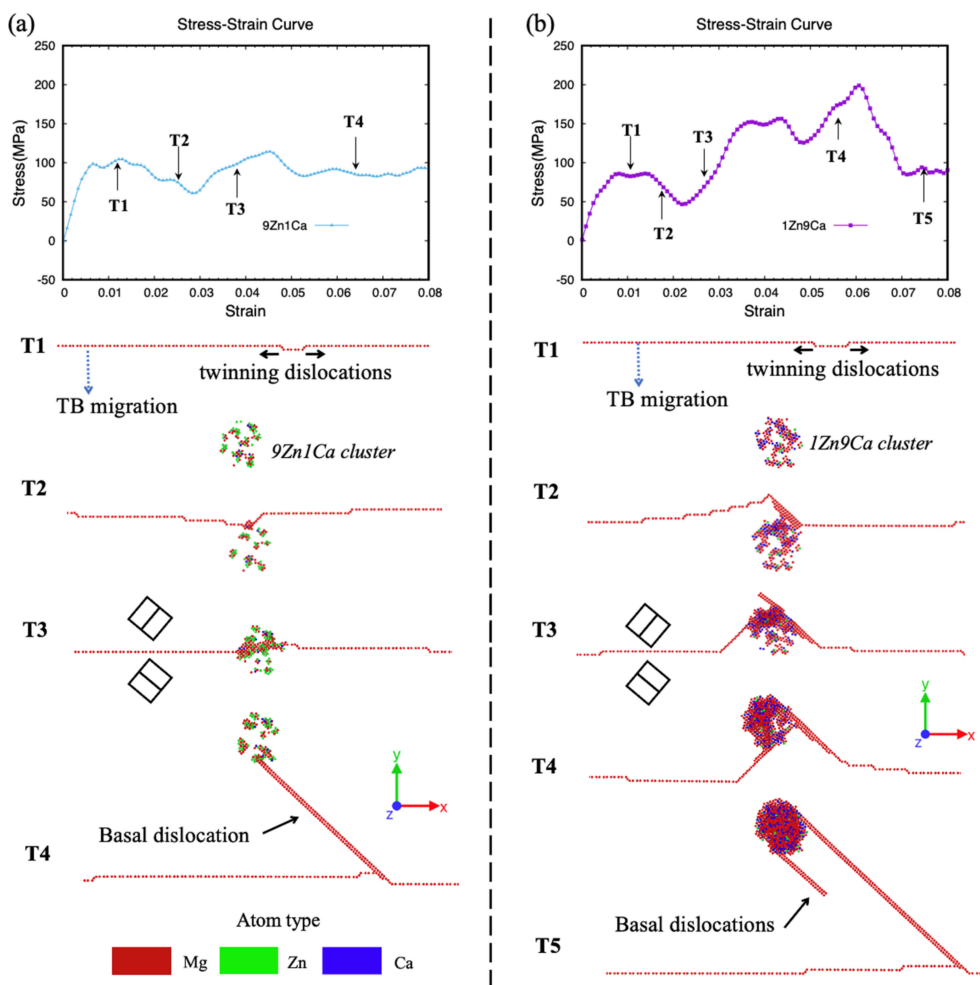


Figure 6. Snapshots showing two interaction events between a TB and a cluster having $R = 2.5$ nm with (a) Zn:Ca = 9:1 and (b) Zn:Ca = 1:9. Atoms sitting at perfect hcp lattice sites are not shown. These figures are sliced at $Z = 0$, while full interaction processes are shown in online Supplemental Movies I and II.

Afterwards, two different ways of interaction are observed. The TB can easily cut through the 9Zn1Ca cluster by leaving a basal dislocation behind, while the TB is significantly tangled with the 1Zn9Ca cluster. The different hardening effect by 9Zn1Ca and 1Zn9Ca clusters is likely a result of the misfit strain due to different atomic radii of Mg (150 pm), Zn (135 pm), and Ca (180 pm) [49]. The larger lattice distortion by the 1Zn9Ca cluster due to the higher concentration of Ca forces plenty of Mg atoms out of their original positions. In fact, more non-perfect hcp atoms are found for the 1Zn9Ca cluster, as shown in Figure 6. The misfit strain caused by the lattice distortion makes it difficult for TB to pass through the 1Zn9Ca cluster, leading to more stress.

It is interesting to notice that, after fully departing from the clusters, trailing dislocations connecting the TB and the cluster are observable. These $\langle a \rangle$ dislocations on basal planes are nucleated from the cluster surface to accommodate the high strain incompatibility between the cluster and twin, leading to a local plastic relaxation once the local stress and misfit strain are sufficiently high [50]. The number of the trailing dislocations increases when Ca dominates the cluster.

From Figure 6, the Ca-rich (1Zn9Ca) cluster has extra resistance against the migration of TBs in Mg-Zn-Ca alloys, indicating a stronger hardening effect than in the Zn-rich (9Zn1Ca) cluster.

4.2. Effect of the Cluster Size and Cluster Concentration

Size is another factor that influences the interactions of clusters with the TB. Stress-strain curves derived from TB interacting with 1Zn9Ca clusters with $R = 1.5, 2.5,$ and 4.0 nm are shown in Figure 7a. It is found that the CRSS of TB migration dramatically reduces to 50 MPa and the $\tau_{\Delta\text{CRSS}}$ rises up to nearly 150 MPa when the cluster has $R = 4.0$ nm. Apparently, the attraction force becomes stronger when increasing the cluster size, and so does the hardening effect.

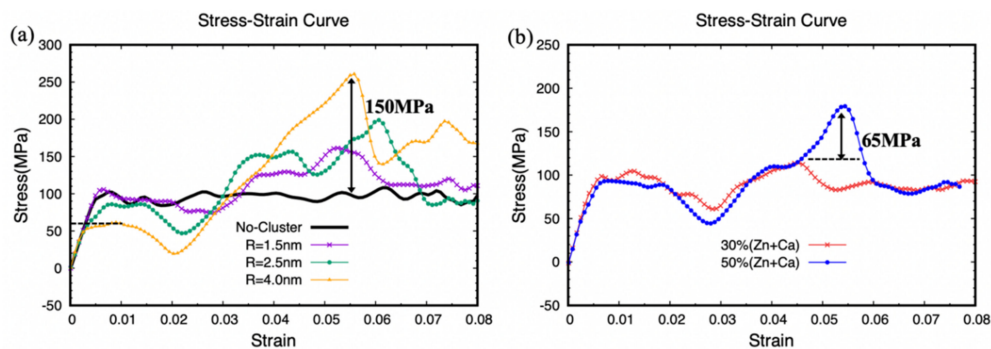


Figure 7. The stress-strain curves of cluster-TB interactions for (a) 1Zn9Ca clusters with a series of cluster radii R . (b) 9Zn1Ca clusters having $R = 2.5$ nm with 30% and 50% (Zn + Ca), respectively.

Moreover, comparing the stress-strain curves for the 9Zn1Ca cluster with $R = 2.5$ nm (Figure 6a) and the 1Zn9Ca cluster with $R = 1.5$ nm (Figure 7a) suggests that the latter exhibits a more pronounced hardening effect. Therefore, the element content is regarded to play a more significant role than the cluster size in terms of hardening.

The effect of cluster concentration was studied as well. As mentioned earlier, the cluster considered here consisted of 70% Mg atoms and 30% (Zn + Ca) atoms to avoid unexpected defects resulting from excessive misfit strain before imposing shear strain. For the 9Zn1Ca case, however, the ratio of (Zn + Ca) can reach 50% without causing additional defects, which is due to the smaller atomic radius of Zn. The stress-strain curves in Figure 7b show that increasing the (Zn + Ca) ratio of the cluster from 30% to 50% can significantly enhance the hardening effect.

5. Conclusions

In this work, to understand the pronounced hardening effects observed experimentally, atomistic simulations are performed to systematically investigate the interactions between clusters and moving $\{10\text{-}12\}$ twinning boundaries in Mg-Zn-Ca alloy. Our simulation results indicate that the cluster produced a hindering effect on TB migration, inducing a significant hardening effect in Mg-Zn-Ca alloy. The following conclusions can be reached:

- (1) Increasing the Ca content can aggravate the lattice distortion of clusters and results in a stronger hardening effect. Furthermore, the cluster hardening effect is also in a positive relationship with the size and concentration of the clusters.
- (2) The attractive effect of clusters on the TB is identified. The attractive force increases with the Ca content and size of the clusters.
- (3) Although the twin boundary is eventually able to bypass the clusters, basal dislocations are left behind, which causes a local plastic relaxation.
- (4) The Zn:Ca ratio in the cluster is found to play a more significant role than the cluster size in impeding TB migration.

Author Contributions: Conceptualization, L.W. and R.L.; methodology, R.L. and J.W.; software, R.L.; validation, R.L., Z.J. and L.W.; formal analysis, R.L.; investigation, R.L.; resources, R.L. and J.W.; data curation, R.L.; writing—original draft preparation, R.L.; writing—review and editing, Z.J. and L.W.; visualization, R.L.; supervision, L.W. and X.Z.; project administration, X.Z.; funding acquisition, X.Z. All authors have read and agreed to the published version of the manuscript.

Funding: This work is funded by the National Natural Science Foundation of China (No. 51825101) and the Shanghai Rising-Star Program (No. 20QA1405000). MD calculations were carried out using the cluster resource ($\pi 2.0$) provided by the HPC Center, Shanghai Jiao Tong University.

Data Availability Statement: Not applicable.

Conflicts of Interest: The authors declare no conflict of interest.

References

1. Bettles, C.; Barnett, M. Introduction. In *Advances in Wrought Magnesium Alloys*; Bettles, C., Barnett, M., Eds.; Woodhead Publishing: Melbourne, Australia, 2012; pp. 12–13, ISBN 978-1-84569-968-0.
2. Pollock, T.M. Weight Loss with Magnesium Alloys. *Science* **2010**, *328*, 986. [[CrossRef](#)] [[PubMed](#)]
3. Christian, J.W.; Mahajan, S. Deformation Twinning. *Prog. Mater. Sci.* **1995**, *39*, 1–157. [[CrossRef](#)]
4. Wang, J.; Hoagland, R.G.; Hirth, J.P.; Capolungo, L.; Beyerlein, I.J.; Tomé, C.N. Nucleation of a (-1012) Twin in Hexagonal Close-Packed Crystals. *Scr. Mater.* **2009**, *61*, 903–906. [[CrossRef](#)]
5. Suh, B.-C.; Shim, M.-S.; Shin, K.S.; Kim, N.J. Current Issues in Magnesium Sheet Alloys: Where Do We Go from Here? *Scr. Mater.* **2014**, *84–85*, 1–6. [[CrossRef](#)]
6. Kim, N.J. Critical Assessment 6: Magnesium Sheet Alloys: Viable Alternatives to Steels? *Mater. Sci. Technol.* **2014**, *30*, 1925–1928. [[CrossRef](#)]
7. Suh, B.-C.; Kim, J.H.; Bae, J.H.; Hwang, J.H.; Shim, M.-S.; Kim, N.J. Effect of Sn Addition on the Microstructure and Deformation Behavior of Mg-3Al Alloy. *Acta Mater.* **2017**, *124*, 268–279. [[CrossRef](#)]
8. Nie, J.F.; Zhu, Y.M.; Liu, J.Z.; Fang, X.Y. Periodic Segregation of Solute Atoms in Fully Coherent Twin Boundaries. *Science* **2013**, *340*, 957. [[CrossRef](#)]
9. Xin, Y.; Zhang, Y.; Yu, H.; Chen, H.; Liu, Q. The Different Effects of Solute Segregation at Twin Boundaries on Mechanical Behaviors of Twinning and Detwinning. *Mater. Sci. Eng. A* **2015**, *644*, 365–373. [[CrossRef](#)]
10. Pei, Z.; Li, R.; Nie, J.F.; Morris, J.R. First-Principles Study of the Solute Segregation in Twin Boundaries in Mg and Possible Descriptors for Mechanical Properties. *Mater. Des.* **2019**, *165*, 107574. [[CrossRef](#)]
11. Hooshmand, M.S.; Ghazisaeidi, M. Solute/Twin Boundary Interaction as a New Atomic-Scale Mechanism for Dynamic Strain Aging. *Acta Mater.* **2020**, *188*, 711–719. [[CrossRef](#)]
12. Vaid, A.; Guérolé, J.; Prakash, A.; Korte-Kerzel, S.; Bitzek, E. Atomistic Simulations of Basal Dislocations in Mg Interacting with Mg17Al12 Precipitates. *Materialia* **2019**, *7*, 100355. [[CrossRef](#)]
13. Liao, M.; Li, B.; Horstemeyer, M.F. Interaction between Prismatic Slip and a Mg17Al12 Precipitate in Magnesium. *Comput. Mater. Sci.* **2013**, *79*, 534–539. [[CrossRef](#)]
14. Fan, H.; Zhu, Y.; El-Awady, J.A.; Raabe, D. Precipitation Hardening Effects on Extension Twinning in Magnesium Alloys. *Int. J. Plast.* **2018**, *106*, 186–202. [[CrossRef](#)]
15. Tang, X.Z.; Guo, Y.F. The Engulfment of Precipitate by Extension Twinning in Mg–Al Alloy. *Scr. Mater.* **2020**, *188*, 195–199. [[CrossRef](#)]
16. Nie, J.F.; Wilson, N.C.; Zhu, Y.M.; Xu, Z. Solute Clusters and GP Zones in Binary Mg–RE Alloys. *Acta Mater.* **2016**, *106*, 260–271. [[CrossRef](#)]
17. Bugnet, M.; Kula, A.; Niewczas, M.; Botton, G.A. Segregation and Clustering of Solutes at Grain Boundaries in Mg–Rare Earth Solid Solutions. *Acta Mater.* **2014**, *79*, 66–73. [[CrossRef](#)]
18. Guo, F.; Pei, R.; Jiang, L.; Zhang, D.; Korte-Kerzel, S.; Al-Samman, T. The Role of Recrystallization and Grain Growth in Optimizing the Sheet Texture of Magnesium Alloys with Calcium Addition during Annealing. *J. Magnes. Alloy.* **2020**, *8*, 252–268. [[CrossRef](#)]
19. Zeng, Z.R.; Bian, M.Z.; Xu, S.W.; Davies, C.H.J.; Birbilis, N.; Nie, J.F. Effects of Dilute Additions of Zn and Ca on Ductility of Magnesium Alloy Sheet. *Mater. Sci. Eng. A* **2016**, *674*, 459–471. [[CrossRef](#)]
20. Pan, H.; Yang, C.; Yang, Y.; Dai, Y.; Zhou, D.; Chai, L.; Huang, Q.; Yang, Q.; Liu, S.; Ren, Y.; et al. Ultra-Fine Grain Size and Exceptionally High Strength in Dilute Mg–Ca Alloys Achieved by Conventional One-Step Extrusion. *Mater. Lett.* **2019**, *237*, 65–68. [[CrossRef](#)]
21. Zhang, A.; Kang, R.; Wu, L.; Pan, H.; Xie, H.; Huang, Q.; Liu, Y.; Ai, Z.; Ma, L.; Ren, Y.; et al. A New Rare-Earth-Free Mg–Sn–Ca–Mn Wrought Alloy with Ultra-High Strength and Good Ductility. *Mater. Sci. Eng. A* **2019**, *754*, 269–274. [[CrossRef](#)]
22. Pan, H.; Kang, R.; Li, J.; Xie, H.; Zeng, Z.; Huang, Q.; Yang, C.; Ren, Y.; Qin, G. Mechanistic Investigation of a Low-Alloy Mg–Ca-Based Extrusion Alloy with High Strength–Ductility Synergy. *Acta Mater.* **2020**, *186*, 278–290. [[CrossRef](#)]
23. Wasiur-Rahman, S.; Medraj, M. Critical Assessment and Thermodynamic Modeling of the Binary Mg–Zn, Ca–Zn and Ternary Mg–Ca–Zn Systems. *Intermetallics* **2009**, *17*, 847–864. [[CrossRef](#)]

24. Zeng, Z.R.; Zhu, Y.M.; Bian, M.Z.; Xu, S.W.; Davies, C.H.J.; Birbilis, N.; Nie, J.F. Annealing Strengthening in a Dilute Mg-Zn-Ca Sheet Alloy. *Scr. Mater.* **2015**, *107*, 127–130. [[CrossRef](#)]
25. Liu, C.; Chen, X.; Chen, J.; Atrens, A.; Pan, F. The Effects of Ca and Mn on the Microstructure, Texture and Mechanical Properties of Mg-4 Zn Alloy. *J. Magnes. Alloy.* **2020**, *9*, 1084–1097. [[CrossRef](#)]
26. Nandy, S.; Tsai, S.P.; Stephenson, L.; Raabe, D.; Zaefferer, S. The Role of Ca, Al and Zn on Room Temperature Ductility and Grain Boundary Cohesion of Magnesium. *J. Magnes. Alloy.* **2021**, *9*, 1521–1536. [[CrossRef](#)]
27. Mostaed, E.; Sikora-Jasinska, M.; Wang, L.; Mostaed, A.; Reaney, I.M.; Drelich, J.W. Tailoring the Mechanical and Degradation Performance of Mg-2.0Zn-0.5Ca-0.4Mn Alloy Through Microstructure Design. *JOM* **2020**, *72*, 1880–1891. [[CrossRef](#)]
28. Wang, J.; Zhu, G.; Wang, L.; Vasilev, E.; Park, J.-S.; Sha, G.; Zeng, X.; Knezevic, M. Origins of High Ductility Exhibited by an Extruded Magnesium Alloy Mg-1.8Zn-0.2Ca: Experiments and Crystal Plasticity Modeling. *J. Mater. Sci. Technol.* **2021**, *84*, 27–42. [[CrossRef](#)]
29. Wang, J.; Zhu, G.; Wang, L.; Zhu, Q.; Vasilev, E.; Zeng, X.; Knezevic, M. Dislocation-Induced Plastic Instability in a Rare Earth Containing Magnesium Alloy. *Materialia* **2021**, *15*, 101038. [[CrossRef](#)]
30. Song, B.; Pan, H.; Ren, W.; Guo, N.; Wu, Z.; Xin, R. Tension-Compression Asymmetry of a Rolled Mg-Y-Nd Alloy. *Met. Mater. Int.* **2017**, *23*, 683–690. [[CrossRef](#)]
31. Nie, J.F.; Shin, K.S.; Zeng, Z.R. Microstructure, Deformation, and Property of Wrought Magnesium Alloys. *Metall. Mater. Trans. A* **2020**, *51*, 6045–6109. [[CrossRef](#)]
32. Tong, L.B.; Zheng, M.Y.; Kamado, S.; Zhang, D.P.; Meng, J.; Cheng, L.R.; Zhang, H.J. Reducing the Tension-Compression Yield Asymmetry of Extruded Mg-Zn-Ca Alloy via Equal Channel Angular Pressing. *J. Magnes. Alloy* **2015**, *3*, 302–308. [[CrossRef](#)]
33. Hidalgo-Manrique, P.; Robson, J.D.; Pérez-Prado, M.T. Precipitation Strengthening and Reversed Yield Stress Asymmetry in Mg Alloys Containing Rare-Earth Elements: A Quantitative Study. *Acta Mater.* **2017**, *124*, 456–467. [[CrossRef](#)]
34. Dobroň, P.; Hegedüs, M.; Olejňák, J.; Drozdenko, D.; Horváth, K.; Bohlen, J. Influence of Thermomechanical Treatment on Tension-Compression Yield Asymmetry of Extruded Mg-Zn-Ca Alloy. In *Magnesium Technology*; Joshi, V., Jordon, J., Orlov, D., Neelameggham, N., Eds.; The Minerals, Metals & Materials Series; Springer: Cham, Switzerland, 2019. [[CrossRef](#)]
35. Yin, D.D.; Boehlert, C.J.; Long, L.J.; Huang, G.H.; Zhou, H.; Zheng, J.; Wang, Q.D. Tension-Compression Asymmetry and the Underlying Slip/Twinning Activity in Extruded Mg-Y Sheets. *Int. J. Plast.* **2021**, *136*, 102878. [[CrossRef](#)]
36. Plimpton, S. Fast Parallel Algorithms for Short-Range Molecular Dynamics. *J. Comput. Phys.* **1995**, *117*, 1–19. [[CrossRef](#)]
37. Jang, H.-S.; Seol, D.; Lee, B.-J. Modified Embedded-Atom Method Interatomic Potentials for Mg-Al-Ca and Mg-Al-Zn Ternary Systems. *J. Magnes. Alloy* **2021**, *9*, 317–335. [[CrossRef](#)]
38. Stukowski, A. Visualization and Analysis of Atomistic Simulation Data with OVITO—the Open Visualization Tool. *Model. Simul. Mater. Sci. Eng.* **2010**, *18*, 015012. [[CrossRef](#)]
39. Luque, A.; Ghazisaeidi, M.; Curtin, W.A. Deformation Modes in Magnesium (0 0 0 1) and (011-1) Single Crystals: Simulations versus Experiments. *Model. Simul. Mater. Sci. Eng.* **2013**, *21*, 045010. [[CrossRef](#)]
40. Dou, Y.; Luo, H.; Zhang, J. The Effects of Yttrium on the {10-12} Twinning Behaviour in Magnesium Alloys: A Molecular Dynamics Study. *Philos. Mag. Lett.* **2020**, *100*, 224–234. [[CrossRef](#)]
41. Esteban-Manzanares, G.; Ma, A.; Papadimitriou, I.; Martínez, E.; Llorca, J. Basal Dislocation/Precipitate Interactions in Mg-Al Alloys: An Atomistic Investigation. *Model. Simul. Mater. Sci. Eng.* **2019**, *27*, 075003. [[CrossRef](#)]
42. Fan, H.; Wang, Q.; Tian, X.; El-Awady, J.A. Temperature Effects on the Mobility of Pyramidal <c+a> dislocations in Magnesium. *Scr. Mater.* **2017**, *127*, 68–71. [[CrossRef](#)]
43. El Kadiri, H.; Barrett, C.D.; Wang, J.; Tomé, C.N. Why Are {101⁻2} Twins Profuse in Magnesium? *Acta Mater.* **2015**, *85*, 354–361. [[CrossRef](#)]
44. Wang, J.; Beyerlein, I.J.; Tomé, C.N. Reactions of Lattice Dislocations with Grain Boundaries in Mg: Implications on the Micro Scale from Atomic-Scale Calculations. *Int. J. Plast.* **2014**, *56*, 156–172. [[CrossRef](#)]
45. Fan, H.; Zhu, Y.; Wang, Q. Effect of Precipitate Orientation on the Twinning Deformation in Magnesium Alloys. *Comput. Mater. Sci.* **2018**, *155*, 378–382. [[CrossRef](#)]
46. Trojanová, Z.; Drozd, D.; Halmešová, K.; Džugan, J.; Škraban, T.; Minárik, P.; Németh, G.; Lukáč, P. Strain Hardening in an AZ31 Alloy Submitted to Rotary Swaging. *Materials* **2021**, *14*, 157. [[CrossRef](#)]
47. Balík, J.; Dobroň, P.; Chmelík, F.; Kužel, R.; Drozdenko, D.; Bohlen, J.; Letzig, D.; Lukáč, P. Modeling of the Work Hardening in Magnesium Alloy Sheets. *Int. J. Plast.* **2016**, *76*, 166–185. [[CrossRef](#)]
48. Máthis, K.; Trojanová, Z.; Lukáč, P. Hardening and Softening in Deformed Magnesium Alloys. *Mater. Sci. Eng. A* **2002**, *324*, 141–144. [[CrossRef](#)]
49. Slater, J.C. Atomic Radii in Crystals. *J. Chem. Phys.* **1964**, *41*, 3199–3204. [[CrossRef](#)]
50. Robson, J.D.; Stanford, N.; Barnett, M.R. Effect of Precipitate Shape on Slip and Twinning in Magnesium Alloys. *Acta Mater.* **2011**, *59*, 1945–1956. [[CrossRef](#)]